This is a post-print (peer-reviewed, corrected) version of OMOSANYA, K.O., HARISHIDAYAT, D. & JOHANSEN, S.E. (2015) Evolution and character of Supra -Sålt Faults in the Easternmost Hammerfest basin, SW Barents Sea. Marine and Petroleum Geology, Volume 66, Part 4, September 2015, Pages 1013-1028. https://doi.org/10.1016/j.marpetgeo.2015.08.010

Evolution and Character of Supra-Salt Faults in the Easternmost Hammerfest basin, SW Barents Sea

Omosanya, K.O., Johansen, S.E., Harishidayat, D.

Group for Interpretation Geophysical Data (IGD)

Department of Petroleum Engineering and Applied Geophysics,

Norwegian University of Science and Technology

Trondheim

1. Introduction

Salt-influenced normal faulting have been documented in various works (e.g., Davison et al., 2000; Stewart, 2006; Wilson et al., 2009; Jackson and Rotevatn, 2013; Perez-Garcia et al., 2013; Reiche et al., 2014). In extensional settings, evaporates can act as decollement surface and influence structural partitioning of sub- and supra-salt deformation (Koyi and Petersen, 1993; Lewis et al., 2013). As a consequence, normal faults developed on salt crest may include crestal, radial, and collapsed crestal graben (Davison et al., 2000; Stewart, 2006). On the other hand, halokinesis can induce normal faulting within salt withdrawal basin (e.g., synclinal faults of Alves et al., 2009).

Structural geologist often collects displacement data in order to unravel the mechanism and kinematic of fault growth (Muraoka and Kamata, 1983; Nicol et al., 1996; Cartwright and Mansfield, 1998; Ferrill and Morris, 2001; Xu et al., 2010). Displacement plots such as displacement versus distance (t-x) (Cartwright and Mansfield, 1998; Baudon and Cartwright, 2008a), displacement versus depth (t-z) (Walsh and Watterson, 1987; Peacock and Sanderson, 1991; Mouslopoulou et al., 2007), expansion and growth indices (Pochat et al., 2009; Thorsen, 1963), and cumulative throw versus age (Omosanya and Alves, 2014) can provide information on fault nucleation, propagation, segmentation and linkage. Despite these numerous works and tools, salt-influenced normal faulting remains an area of continuing interest and research to both the academia and exploration industry.

The study area lies at the boundary of the Hammerfest and Nordkapp Basin in SW Barents Sea, the area of interest extend from the domain of the salt-influenced Masøy Fault Complex into the Finnmark Fault Complex (Figure 1). This area presents a unique opportunity to investigate the character of salt-influenced normal faulting. The aim of this paper is to describe and assess the displacement character of supra-salt normal faults in the Easternmost Hammerfest Basin. To achieve this aim, we use displacement plots to reconstruct the history of fault and salt growth. We demonstrate that the technique used remains relevant to fault analysis. In the discussion section, history of faults and salt growth were discussed and their implication for hydrocarbon exploration.

2. Regional Geology

The Eastern Hammerfest Basin is part of the Barents Sea, an epicontinental Sea on the northwestern margin of the Eurasian continental shelf (Faleide et al., 1993). Tectonic development of several basins in the Barents Sea is linked to the Caledonian orogeny of *c*. 400 Ma and collision of Laurasian continent and western Siberia at *c*. 240 Ma (Doré, 1995, 1991; Faleide et al., 2008; Smelror et al., 2009). Evolution of the Barents Sea before the Carboniferous remains a subject of ongoing research and debate as the entire Barents Sea area developed through multiple and complex orogenies including Timanian, Caledonian, Uralian, proto-Atlantic rifting and breakup of northern North Atlantic margin (Doré, 1991; Faleide et al., 1984; Gernigon et al., 2014; Gudlaugsson et al., 1998; Johansen et al., 1994; Worsley, 2008). As a result, post- Carboniferous deformation in the entire Barents Sea reflects inherited basement structure, older Precambrian suture and Caledonian configuration (Barrère et al., 2009; Gernigon et al., 2014). Five basement rock types were identified and described in SW Barents Sea based on potential field data (Barrère et al., 2009). The Eastern Hammerfest Basin is characterized by B1 basement of Archaean to Paleoproterozoic age with the overlying rocks and structures ranging in age from Paleozoic to Quaternary.

The oldest rifting event of late Devonian to early Carboniferous resulted in the formation of Nordkapp, Maud, Fingerdjupet, Tromsø and Ottar Basins. Rift basins in the Barents Sea Shelf were formed during this rifting and those of Permian, Triassic, and Late Jurassic/Early Cretaceous times (Glørstad-Clark et al., 2010; Johansen et al., 1994). Silurian to Early Devonian witnessed large-scale erosion and exhumation of Caledonian highs (Smelror et al., 2009). Evaporites were deposited in most southwestern basins of the Barents Sea in Late Carboniferous with most of the salt diapirs developed in Late Triassic (Nilsen et al., 1995). Transgressive to regressive cycles of marine, deltaic and continental clastics were deposited in lower to middle Triassic (Glørstad-Clark et al., 2010). Late Triassic to Early Cretaceous times were characterized by post-rift thermal subsidence, rifting and renewed tilting of blocks (Faleide et al., 1993; Worsley, 2008). The northern progradation of Atlantic rifting in Middle Jurassic to Early Cretaceous affected the western margin of the Barents Sea Shelf and prompted subsequent growth of a marine connection across the shelf (Tsikalas et al., 2012).

Cretaceous rifting and sedimentation are revealed as NE-SW oriented structures and thick strata in Bjørnøya Basin with Late Cretaceous folding and faulting recorded in the Senja Ridge. During this time, platform uplift was predominant along the entire Barents Sea. As a consequence, large amount of sediments were abraded from uplifted continental areas in the NW and deposited in several subsiding basins in the west (Riis et al., 1986; Worsley, 2008). Tertiary deformation includes wrench movement along SW to NE trends and progressive formation of pull-apart basins in the westernmost parts of the Barents Sea (Fiedler and Faleide, 1996; Gernigon et al., 2014). Neogene glaciations in the northern hemisphere caused intense erosion, uplift and deposition of thick sediments in oceanic basins north and west of the Barents Sea (Faleide et al., 1996).

3. Data and Methods

The main data for this work is a post stack time migrated (PSTM) 3D seismic cube covering *c*. 865 km^2 acquired on the continental shelf of Eastern Hammerfest Basin (Figure 1). The seismic cube has inline and crossline spacing of *c*.19 m and *c*.12.5m, with a recording length and vertical sampling rate of 4500 ms and 4 ms, respectively. Using a dominant frequency of 40 Hz and average velocity of 2500 m/s, vertical and horizontal resolutions are *c*. 15.6 m and *c*. 12.5 m. In addition, three 2D lines BSS01-203, BSS01-204, BSS01-205 were used to understand the location of seismic cube within the context of the regional geology (Figures 1a and 3).

Stratigraphic correlation was done to regional column of Mørk et al., 1999 and Glørstad-Clark et al., 2010 (Figure 2) while lithology and ages of horizons were calibrated using borehole 7125/4-1 and 7125/4-2 drilled by Norsk Hydro Produksjon AS and Statoil Hydro Petroleum AS (Figure 3). An additional borehole 7123/3-1 along one of the 2D lines was used to establish the age of the Paleozoic units (Figure 1b).

Seismic interpretation includes horizon, fault mapping and seismic attribute analysis. Eight regional unconformities were interpreted in the entire seismic cube while seven other horizons were locally mapped during fault analysis. These horizons were named H1 to H15 (Figures 3 to 6). Based on these horizons, the study area was further divided into four main stratigraphic units ranging in age from Paleozoic age (Unit 4) to Cenozoic (Unit 1). Faults were imaged using variance maps (Figure 4). Variance is the direct measurement of dissimilarity of seismic traces. Variance maps convert a volume of continuity into a volume of discontinuity, highlighting structural and stratigraphic boundaries (Brown, 2004). Faults represent trace-to-trace variability and are mapped with high variance coefficient. Fifty-three faults were interpreted in the study area. The orientation of the faults is graphically presented using a rose diagram in Figure 4.

Fault propagation and evolution were assessed using displacement plots and expansion indices. Throw values were estimated on faults using seismic profiles perpendicular to fault strike (Mansfield and Cartwright, 1996). The throw is the difference between hangingwall and footwall cut-offs. Expansion index (EI) is the ratio of thickness between the layers in the hangingwall to the thickness in the footwall of a fault (Pochat et al., 2009; Thorsen, 1963) while the growth index is calculated as the difference in thickness between the hangingwall and the footwall of an interval divided by the thickness of the interval in the footwall (Childs et al., 2003). Errors in throw estimate were dependent on the vertical sampling rate of 4 ms (see Baudon and Cartwright, 2008b). All the fifty-three faults were analyzed for their scaling character i.e. maximum displacement versus fault length (Figure 10). For the plots of throw vs. depth, throw vs. distance, expansion and growth indices, and throw against the ages of horizons, nine representative faults were interpreted and named F1 to F9 (Figures 8 to 12).

4. Seismic and litho-stratigraphy

The seismic character of the four principal stratigraphic units comprising horizons H1 to H15 are summarized in Table 1.

Unit 1 (H1 to H2)

On seismic profiles, unit 1 includes low amplitude reflection at its base, continuous high amplitude reflections in the middle and very low amplitude reflections towards the sea bed (Figure 4). Unit 1 comprises the Nordland Group, which is characterized by marine claystones, siltstone and sandstone (Dalland et al., 1988; Glørstad-Clark et al., 2010; Mørk et al., 1999). Claystones facies may include grey, greenish-grey and grey-brown, soft, locally silty and micaceous. Unit 1 is Quaternary to Tertiary in age.

Unit 2 (H2 to H4)

Seismic characters in this unit include homogeneous, very low amplitude and continuous reflections (Figures 4 and 5). Lithologically, the units include Kolmule and Kolje Formation. Rocks of Kolmule Formation are dark grey to green claystone and shale, silty in parts with minor thin siltstone interbeds with limestone and dolomite stringers (Dallan et al., 1988). Average thickness of the Formation is c. 530m in borehole 7125/4-1 and 7125/4-2 respectively (Figure 3). The Kolje Formation is composed of similar lithology as described in the Kolmule Formation except that Kolje Formation has an average thickness of c. 103m in the two boreholes (Figure 3).

Unit 3 (H4 to H11)

Unit 3 is reflected as very continuous, moderate to low amplitude reflections at the base (H11), continuous and moderate to high amplitude reflections at the middle (H7 to H9; Kobbe to Klappmyss Formation) and closely-spaced, continuous and high amplitude reflectors at the upper part i.e. horizons H7 to H5 (Fruholmen and Snadd Formation; Figures 2, 4).

In borehole 7145/4-2, the Fruholmen Formation is c. 221 m thick and includes grey to dark grey shales at the base and interbedded sandstones, shales and coals (Dalland et al 1988). On the other hand, the Snadd Formation is composed of coarsening upward sequence which includes grey shales at the base and coarse shales with interbeds of grey siltstones and sandstones towards the top (Mørk et al., 1999; Glørstad-clark et al 2010). Limestones and calcareous interbeds are quite common in the lower and middle parts of the unit, while thin coaly lenses are developed locally further up. Distinctive dusky red-brown shales occur near the top of the unit (Mørk et al., 1999; Glørstad-clark et al 2010).

On seismic profile, the Kobbe Formation occurs within the interval H7 and H8 (Figure 4). Lithologic composition of the Formation includes 20 m thick shale at its base which passes up into interbedded shale, siltstone and carbonate cemented sandstone (Dallan et al., 1988). Average thickness of the Kobbe Formation is c. 283m (Figure 3). The Klappmyss interval is defined by Horizons H9 and H10 and is composed of medium to dark grey shales which grades upwards into interbedded shales, siltstones and sandstones in borehole 7125/4-2 (Figure 3). Average thickness of this Formation is c.427m. Unit 3 is dated Triassic age (Dallan et al., 1988).

Unit 4 (H11 to base of data)

This unit is not penetrated by the boreholes. However, horizon H13 correlates to a regional unconformity above the carbonate platform (Figures 1b and 3). On seismic profiles, unit 4 is indicated by moderate to high amplitude reflection at its upper part and discontinuous, moderate to high amplitude reflections at the base (Figures 4, 5 and 7). The upper part of this unit is defined by horizon, H11. Unit 4 may include other Paleozoic rocks of Tempel Fjorden and Billiefjorden groups (Mørk et al., 1999; Glørstad-clark et al 2010). On the present seismic cube, the top evaporate is inferred at depth of c. 2550 ms to 3000 ms (TWTT) occurring especially in the western and southern part of the data (Figures 4 to 6).

4.1 Faults in the study area

Faults in the study include both crestal (e.g., F1 and F2) and synclinal faults (e.g., F3, F4, and F5). The crestal faults are located close to the crest of the salt diapirs while synclinal faults are normal faults located within the withdrawal basins on the salt flank (Figures 4 to 7). Faults geometry includes synthetic and antithetic faults forming graben and half-grabens with orientation in NE-SW, E-W and NW-SE directions

(Figure 4 and 5). In terms of the location of their upper tips, faults in the study area include a) those faults that intersected the Cretaceous units (F4, F5, F8 and F9) b) faults that are restricted to the Jurassic and Triassic interval (F3, F6 and F7) and c) faults extending from Cretaceous to and deeper into the Paleozoic unit (F1 and F2). Fault density increases toward the south western part of the seismic cube where they produced depression characterized by thickness variation associated with uplifted and subsided footwall and hanging wall blocks (Figure 6). Away from this depression, the studied interval was insignificantly faulted and composed of small-scale faults within Unit 1 and 2. These are understood as subtle normal faults observed within the Cretaceous interval (Figure 7). The latter fault types exhibit polygonal pattern in map view (Figure 7c). However, it should be noted that these faults and those that are limited to the Paleozoic units were not investigated for their displacement character.

4.2 Displacement analyses

Displacement-distance (t-x) plots

The t-x profiles for the faults vary from simple to complicated curves including triangular (F1 and F4), asymmetric (F2, F7 and F9), symmetric (F3 and F5) and flat-topped curves (F6 and F8). Except for faults F1, F2 and F4, other faults have more steeply sloping boundaries (Figure 8). In addition, the complexity of the throw profiles is derived from the presence of several subunits which are delimited by local displacement minima (Figure 8). The subunits are considered segments that were linked at the local minima during fault growth (Walsh et al., 2003). As a consequence, the local maxima coincide with the point of fault nucleation for individual segments. The maximum displacement (d_{max}) ranges from 20 m (F3) to 425 m (F5) with the maximum fault length of c. 19 km for F5. Fault F1 and F2 have maximum length of c.

17 km and 19 km at this level (Figure 8). In addition, the number of segments varies amongst faults. For example, two segments were inferred for F3, F7 and F8 while the faults with the highest number of segments are F2 and F4 in which thirteen subunits/segments were interpreted (Figure 8).

Throw-depth (t-z) plots

Throw versus depth plots are shown in two-way travel time (TWTT; Figure 9). Throw plots presented in time are not considerably different in geometry from those in depth (Baudon and Cartwright, 2008a; Tvedt et al., 2013). The throw profiles include C-type (F3, F9), M-type (F6, F7 and F8) both of (Muraoka and Kamata, 1983), Skewed M-type (F1, F4 and F5) and asymmetric-type (F2). The faults show a) consistent upward increase and decrease in throw with depth and b) amalgamated throw profile linked by throw minima. Throw minima in this work is described as the minimum throw value located not at the upper and lower tips of the throw-depth profile.

The maximum displacement (d_{max}) varies across horizons and inconsistently with depth. For F1, d_{max} is located on H9, H10 for F4, H7 for F7 and so on (Figure 9). The faults with distinctive local throw minima include F5 and F9. The throw minima separate an asymmetric profile from a skewed M-type profile for F4 (Figure 9) while two points of localized minimum throw were determined for F9 in which a C-type profile is sandwiched within two skewed M-type curves (Figure 9).

Displacement scaling (d_{max} vs. L)

The best-fit curve for the plot of displacement against the length of fault is along H5 and it is a power-law relationship with a correlation coefficient of 0.7 and exponent of

~ 1 (Figure 10a). For the horizons H6 and H7, the correlation coefficient is 0.6 and 0.5, respectively (Figure 10b and c). The best-fit for linear curves have correlation coefficients of 0.7, 0.8 and 0.1 along H5, H6 and H7. Conversely, exponential curves have correlation coefficient of less than 0.5 in all cases (Figure 10a-c). In general, all the faults have displacement three orders less than their length along strike. There is a cluster of plots around D:L of 1E+2 to 1E+4 (Figure 10 a-c). The displacement to length ratio ranges from 0.1 to 0.4.

Cumulative throw versus age

In order to estimate the timing of reactivation in the study area, cumulative throw of the faults were plotted against the ages of the horizons intersected (Omosanya and Alves, 2014). The plot was obtained at the same point and interval as t-z plots. Highest cumulative throw was obtained for F2 with throw of c. 2635 ms TWTT (3952 m) while the lowest value was estimated for F6 with throw of 92 ms TWTT (138 m). Curves for the entire nine faults include smooth and bridged curves that are characterized by several skips (Figure 10 d-f). The most consistent skip is observed between horizon H5 and H6. Other skips or steps in the curve include along H8 and H9, H10 and H11, H3 and H4, and between H6 and H7 (Figure 10 d-f).

4.3 Expansion and Growth Indices

Faults in the study area are characterized by expansion index (EI) of greater 1.0 (Figure 11). The highest value of 1.3 was estimated for F2 whereas the lowest value of 1.01 was calculated for F3 and F6, respectively (Figure 11). Different pattern in variation of expansion index with depth was observed for each of the faults. For instance, F3, F7, F5, F8 and F9 show asymmetrical values of EI with depth i.e. the values of EI increase and then gradually decrease towards the uppermost horizon (Figure 11). Only F4 show a consistent upward increase in thickness of its hangingwall with depth from its lower to upper tips. In addition, the highest variation in thickness from hanging wall to footwall was estimated for horizon, H5 for all the faults except F1, F2 and F3 (Figure 11).

For growth indices (GI), faults F3, F4, F6, F8 and F9 are marked by growth index of less than 0.1 (Figure 12). Other faults display a combination of less than 0.1 and greater than 0.1. Fault, F2 show absolutely GI of > 0.1 across all the interpreted horizons, with the least value estimated on horizon, H8 for this particular fault. For the other faults with GI > 0.1, the growth index varies across all horizons. For example, the highest value of GI is at horizon H11 for F2, H5 for F5 and H9 for F1.

5.0 Discussion

5.1 Tectonic evolution of faults

Evidence from isopach maps of Figure 6 show that the interpreted faults were characterized by significant thickness variation or stratigraphic thickening within the depression. We hypothesize that a) F1 and F2 are segments of the regional Finnmark and Masøy Fault complex (Figure 1). The depression is therefore considered a collapse graben bounded by listric fault F1 and F2 (Figures 4 and 5). Other faults are component of the collapse structure which was presumably developed when the rollover anticline associated with these listric faults was breached. So, F1 and F2 are detached onto the evaporitic decollement surface. Although the displacement plot of Fault F2 was terminated at depth c. 1800 ms TWTT, Figure 5. The presence of other faults at this depth may suggest that F2 was not a single fault but part of a ductile strand that are kinematically linked over the crest of the salt structure (e.g., Koyi and Petersen, 1993; Koyi et al., 1993; Lewis et al., 2013b). Fault F2 may therefore extend beyond the interpreted lower tip or dip linked with additional faults at depth. Alternatively, we consider all the faults as supra-salt faults developed on a supposedly deflated salt anticline.

Stratigraphic thickening within the depression implied coeval sedimentation with fault growth (cf. Childs et al., 2003; Freeth and Ladipo, 1986; Wilson et al., 2009). The expansion indices of these faults show that all the faults are characterized by major thickening in their down-thrown section and therefore are syn-sedimentary faults. However, the growth indices suggest that the faults were buried at some point during their growth. Fault with GI < 0.1 were not exposed during their formation. Conversely, GI > 0.1 suggests that the fault interacted with a free surface while growing. Therefore, Fault F2 with GI of > 0.1 at all interpreted surface is distinctly a syn-sedimentary fault while F1 and F5 with combined GI greater and less than 0.1 were buried and subsequently exposed during their growth. This is evidence for polycyclic faulting during the growth of the faults (*cf.* Jackson and Rotevatn, 2013; Tvedt et al., 2013). To further buttress this point, F1 and F5 are characterized by upward increase in throw with depth (Figure 9) and therefore are diagnostic and classic examples of fault developed through syn-sedimentary activity (Childs et al., 2003). For F2 instead, the t-z profile revealed an upward decrease in throw with depth, characteristic of fault developed through blind propagation of their tip (Barnett et al., 1987). This behavior indicates that F2 was exposed at a free surface during its evolution but grew by blind propagation of its tips. Hence, buried fault (i.e. blind fault) may grow either through blind propagation of their tips or by syn-sedimentary activity (Nicol et al., 1996).

As for timing of faulting, we hypothesize faults in the study area were formed as of the deposition of the latest Paleozoic unit, H13. Some of the faults have their lower tips extended to this surface (Figures 4 and 5). The entire faults developed with sedimentation and at different times were exposed at or buried beneath stratigraphic surface. Furthermore, the site of nucleation is variable among the faults provided the location of d_{max} is the point of fault nucleation and propagation (Barnett et al., 1987; Nicol et al., 1996; Walsh and Watterson, 1987). For example, the position of d_{max} for F4 and F9 is at horizon H10, horizon H5 for F5 and F8, horizon H9 for F1 and F3 and at different depth for the other faults. The point of maximum displacement can vary as a function of lithological heterogeneity, fault linkage and segmentation (Cowie, 1998; Peacock and Sanderson, 1991). Since, the fault in this study exhibit complex segmentation (Figure 8), their d_{max} position may not necessarily be the point of nucleation. The effect of lithology heterogeneity on fault growth is evidenced by the displacement scaling factor (Figure 10 a-c). The interpreted faults show that there is a strong control of lithology on their propagation as the exponent of the power-law varies accordingly with the horizons (See also Kim and Sanderson, 2005; Schlische and Anders, 1996 for the effect of lithology on the displacement length scaling). Hence, faults in the study area are good examples of faults whose propagation is dependent on the composition of the interval intersected.

Evidence for fault reactivation is shown by skips/jumps in the cumulative throw versus age plot (Figure 10 d-f) and throw-depth plot of Figure 8. The dominant/

consistent skips are noted at horizons H5 and H6 (Late Triassic), H8 and H9 (Early Triassic), and H10 and H11 (Early Triassic). The less frequent steps include those along H6 and H7 (Middle Triassic) and lastly between H3 and H4 (Early Cretaceous). Hence, we propose that fault reactivation could have taken place during these times especially during the interval between the dominant skips. The greatest limitation of this timing is the age of horizons used for the cumulative plot. The ages are fairly chosen based on well tops from the boreholes and by correlation to similar regional surfaces. Hence, we exercise some restraint in taking these ages as absolute time of regional fault reactivation. Furthermore, the mode of fault reactivation is through dip linkage as shown by the t-z plot of F2 and F9, respectively (cf. Mansfield and Cartwright, 1996). Throw minima on these plots correspond to the point where numerous isolated faults are connected into one single fault after accumulating displacement over time.

5.2 Timing of salt growth in the study area

As discussed earlier under the section on regional geology, evaporites are deposited in most basins in the Barents in Carboniferous times. On the eastern section of the study area i.e. southwest of the Nordkapp Basin, the history of halokinesis has been documented by several workers (e.g., Gabrielsen et al., 1992; Jensen and Sørensen, 1992; Hemin Koyi et al., 1993; Talbot et al., 1993). However, effects of halokinesis on basin fill in the Hammerfest Basin are sparingly reported. Since the principal faults F1 and F2 are located on the crest of the salt structure and also show thickening of Paleozoic and Triassic strata (EI 1.08 to 1.30; Figure 11), we postulate that halokinesis or salt rise influenced crestal faulting as early as Mid to Late Paleozoic. This time coincided with the earliest stage of salt rise. The other faults developed mainly through Triassic period in response to continued salt rise or movement. Towards the latest Triassic times, considerable thickening was recorded along horizon, H5 with expansion index reaching up to 1.22 (Figure 11). This may signify deflation of the salt structure as the space offered by the salt is compensated with sediment of late Triassic age. Reactivation of faults and their extension up to the Cretaceous interval could also have been affected by the salt movement or regional tectonics. Hence, salt rise in the study area was recorded from Late Paleozoic possibly Permian through Triassic to Late Cretaceous times.

5.3 Implication for hydrocarbon exploration

Fault systems influenced by or related to salt movement are characterized by important accommodation zone (Kane et al., 2010; Stewart and Clark, 1999). The later zones are important for migration of hydrocarbon across barriers. We have shown that the collapse graben or supra-salt fault discussed in this work exhibit significant stratigraphic thickening and complex lateral segmentation, hence high accommodation zones are presented along the fault system. Since the faults also show prominent juxtaposition across hangingwall and footwall section, with throw reaching up to 1300 m. This may imply the faults are good seals or barriers to fluid flow. Although reactivated faults are most likely leaky barriers to flow fluid flow (*cf.* Wiprut and Zoback, 2000). However, with the complex architecture of the faults, the large variation in displacement along strike, and the presence of good accommodation zones within the fault system, the study area hold promise for commercial hydrocarbon exploration.

6.0 Conclusions

Faults in the study area are part of a collapse graben. The fault systems are developed as the rollover anticline ruptured during salt halokinesis. Faults in the study area have evolved since late Paleozoic and developed through Triassic to Early Cretaceous time. They are characterized by simple to complex lateral segmentation with prominent displacement variation along strike. In addition, some of the faults exhibit polycyclic growth involving transition between blind propagation and syn-sedimentary activity during their evolution. Fault reactivation is through dip-linkage which was more predominant in Early to Late Triassic times. Displacement scaling for these faults is a power-law relationship with an exponent of 1. Across stratigraphy, the coefficient of correlation for this scaling varies as a function of differing mechanical property of the interval intersected by the faults. In addition, associated with complex fault segmentation is the presence of accommodation zones that are important during hydrocarbon migration.

Acknowledgement

We appreciate the financial support of Research Centre for Arctic Petroleum Exploration (ARCEX) and Multi Client Geophysical (MCG) towards the successful completion of this research. The Norwegian Petroleum Directorate (NPD) is greatly appreciated for access to the datasets used for this research and Schlumberger for provision of Petrel® and RDR plugin.

References

Alves, T.M., Cartwright, J., Davies, R.J., 2009. Faulting of salt-withdrawal basins during early halokinesis: Effects on the Paleogene Rio Doce Canyon system

(Espírito Santo Basin, Brazil). AAPG Bull. 93, 617–652. doi:10.1306/02030908105

Barnett, J.A., Mortimer, J., Rippon, J.H., Walsh, J.J., Watterson, J., 1987. Displacement geometry in the volume containing a single normal fault. AAPG Bull. 71, 925–937.

Barrère, C., Ebbing, J., Gernigon, L., 2009. Offshore prolongation of Caledonian structures and basement characterisation in the western Barents Sea from geophysical modelling. Prog. Underst. Sediment. Basins 470, 71–88. doi:10.1016/j.tecto.2008.07.012

Baudon, C., Cartwright, J., 2008a. The kinematics of reactivation of normal faults using high resolution throw mapping. J. Struct. Geol. 30, 1072–1084. doi:10.1016/j.jsg.2008.04.008

Baudon, C., Cartwright, J.A., 2008b. 3D seismic characterisation of an array of blind normal faults in the Levant Basin, Eastern Mediterranean. J. Struct. Geol. 30, 746–760. doi:10.1016/j.jsg.2007.12.008

Brown, A.., 2004. Interpretation of Three-Dimensional Seismic Data, Sixth. ed. American Association of Petroleum Geologists (AAPG), Tulsa.

Cartwright, J.A., Mansfield, C.S., 1998. Lateral displacement variation and lateral tip geometry of normal faults in the Canyonlands National Park, Utah. J. Struct. Geol. 20, 3–19. doi:10.1016/S0191-8141(97)00079-5

Childs, C., Nicol, A., Walsh, J.J., Watterson, J., 2003a. The growth and propagation of synsedimentary faults. J. Struct. Geol. 25, 633–648. doi:10.1016/S0191-8141(02)00054-8

Childs, C., Nicol, A., Walsh, J.J., Watterson, J., 2003b. The growth and propagation of synsedimentary faults. J. Struct. Geol. 25, 633–648.

Cowie, P.., 1998. Normal fault growth in three-dimensions in continental and oceanic crust, in Faulting and Magmatism at Mid-Ocean Ridges: Geophys. Monogr., American Geophysical Union 106, 325–348.

Dalland, A., Worsley, D., Ofstad, K., 1988. A lithostratigraphic scheme for the Mesozoic and Cenozoic succession offshore mid- and northern Norway. NPD Bull. 4.

Davison, I., Alsop, G.., Evans, N.., Safaricz, M., 2000. Overburden deformation patterns and mechanisms of salt diapir penetration in the Central Graben, North Sea. Mar. Pet. Geol. 17, 601–618. doi:10.1016/S0264-8172(00)00011-8

Doré, A.., 1995. Barents Sea Geology, Petroleum Resources and Commercial Potential. Arctic 48, 207–221.

Doré, A.G., 1991. The structural foundation and evolution of Mesozoic seaways between Europe and the Arctic. Palaeogeogr. Paleoceanogr. Tethys 87, 441–492. doi:10.1016/0031-0182(91)90144-G

Faleide, J.I., Gudlaugsson, S.T., Jacquart, G., 1984. Evolution of the western Barents Sea. Mar. Pet. Geol. 1, 123–150. doi:10.1016/0264-8172(84)90082-5

Faleide, J.I., Solheim, A., Fiedler, A., Hjelstuen, B.O., Andersen, E.S., Vanneste, K., 1996. Late Cenozoic evolution of the western Barents Sea-Svalbard continental margin. Impact Glaciat. Basin Evol. Data Models Nor. Margin Adjac. Areas 12, 53–74. doi:10.1016/0921-8181(95)00012-7

Faleide, J.I., Tsikalas, F., Breivik, A.J., Mjelde, R., Ritzmann, O., Engen, Ø., Wilsom, J., Eldholm, O., 2008. Structure and evolution of the continental margin off Norway and the Barents Sea. Episodes 31, 82–91.

Faleide, J.I., Vågnes, E., Gudlaugsson, S.T., 1993. Late Mesozoic-Cenozoic evolution of the south-western Barents Sea in a regional rift-shear tectonic setting. Mar. Pet. Geol. 10, 186–214. doi:10.1016/0264-8172(93)90104-Z

Ferrill, D.A., Morris, A.P., 2001. Displacement gradient and deformation in normal fault systems. J. Struct. Geol. 23, 619–638. doi:10.1016/S0191-8141(00)00139-5

Fiedler, A., Faleide, J.I., 1996. Cenozoic sedimentation along the southwestern Barents Sea margin in relation to uplift and erosion of the shelf. Impact Glaciat. Basin Evol. Data Models Nor. Margin Adjac. Areas 12, 75–93. doi:10.1016/0921-8181(95)00013-5

Freeth, S.J., Ladipo, K.O., 1986. The development and restoration of syn-sedimentary faults. Earth Planet. Sci. Lett. 78, 411–419. doi:10.1016/0012-821X(86)90007-5

Gabrielsen, R.H., KlØvjan, O.S., Rasmussen, A., Stølan, T., 1992. Interaction between halokinesis and faulting: structuring of the margins of the Nordkapp Basin, Barents Sea region, in: Talleraas, R.M.L.B.T.L. (Ed.), Structural and Tectonic Modelling and Its Application to Petroleum Geology. Elsevier, Amsterdam, pp. 121–131.

Gernigon, L., Brönner, M., Roberts, D., Olesen, O., Nasuti, A., Yamasaki, T., 2014. Crustal and basin evolution of the southwestern Barents Sea: From Caledonian orogeny to continental breakup: Evolution of the Barents Sea. Tectonics 33, 347–373. doi:10.1002/2013TC003439

Glørstad-Clark, E., Faleide, J.I., Lundschien, B.A., Nystuen, J.P., 2010. Triassic seismic sequence stratigraphy and paleogeography of the western Barents Sea area. Mar. Pet. Geol. 27, 1448–1475.

Brdoi:10.1016/j.marpetgeo.2010.02.008

Gudlaugsson, S.T., Faleide, J.I., Johansen, S.E., Breivik, A.J., 1998. Late Palaeozoic structural development of the South-western Barents Sea. Mar. Pet. Geol. 15, 73–102. doi:10.1016/S0264-8172(97)00048-2

Jackson, C.A.-L., Rotevatn, A., 2013. 3D seismic analysis of the structure and evolution of a salt-influenced normal fault zone: A test of competing fault growth models. J. Struct. Geol. 54, 215–234. doi:10.1016/j.jsg.2013.06.012

Jensen, L.N., SØrensen, K., 1992. Tectonic framework and halokinesis of the Nordkapp Basin, Barents Sea, in: Larsen, R.M., Brekke, H., Larsen, B.T., Talleraas, E. (Eds.), Structural and Tectonic Modelling and Its Application to Petroleum Geology. Elsevier, Amsterdam, pp. 109–120.

Johansen, S.E., Henningsen, T., Rundhovde, E., Sæther, B.M., Fichler, C., Rueslåtten, H.G., 1994. Continuation of the Caledonides north of Norway: seismic reflectors within the basement beneath the southern Barents Sea. Mar. Pet. Geol. 11, 190–201. doi:10.1016/0264-8172(94)90095-7

Kane, K.E., Jackson, C.A.-L., Larsen, E., 2010. Normal fault growth and fault-related folding in a salt-influenced rift basin: South Viking Graben, offshore Norway. J. Struct. Geol. 32, 490–506. doi:10.1016/j.jsg.2010.02.005

Kim, Y.-S., Sanderson, D.J., 2005. The relationship between displacement and length of faults: a review. Earth-Sci. Rev. 68, 317–334. doi:10.1016/j.earscirev.2004.06.003

Koyi, H., Jenyon, M.., Petersen, K., 1993. The effect of basement faulting on diapirism. J. Pet. Geol. 16, 285–312.

Koyi, H., Petersen, K., 1993. Influence of basement faults on the development of salt structures in the Danish Basin. Mar. Pet. Geol. 10, 82–94. doi:10.1016/0264-8172(93)90015-K

Koyi, H., Talbot, C.J., Tørudbakken, B.O., 1993. Salt diapirs of the southwest Nordkapp Basin: analogue modelling. Tectonophysics 228, 167–187. doi:10.1016/0040-1951(93)90339-L

Lewis, M.M., Jackson, C.A.-L., Gawthorpe, R.L., 2013a. Salt-influenced normal fault growth and forced folding: The Stavanger Fault System, North Sea. J. Struct. Geol. 54, 156–173. doi:10.1016/j.jsg.2013.07.015

Lewis, M.M., Jackson, C.A.-L., Gawthorpe, R.L., 2013b. Salt-influenced normal fault growth and forced folding: The Stavanger Fault System, North Sea. J. Struct. Geol. 54, 156–173. doi:10.1016/j.jsg.2013.07.015

Mansfield, C.S., Cartwright, J.A., 1996a. High resolution fault displacement mapping from three-dimensional seismic data: evidence for dip linkage during fault growth. J. Struct. Geol. 18, 249–263.

Mansfield, C.S., Cartwright, J.A., 1996b. High resolution fault displacement mapping from three-dimensional seismic data: evidence for dip linkage during fault growth. J. Struct. Geol. 18, 249–263.

Mørk, A., Dallmann, W., Dypvik, H., Johannesen, E.., Larssen, G.., Nagy, Nøttvedt, A., Olaussen, S., Pc elina, T.., Worsley, D., 1999. Mesozoic lithostratigraphy., in: In W.K. Dallmann (ed.): Lithostratigraphic Lexicon of Svalbard. Upper Palaeozoic to Quaternary Bedrock. Review and Recommendation for Nomenclature Use. Norwegian Polar Institute., Tromsø, pp. 127–214.

Mouslopoulou, V., Nicol, A., Little, T.A., Walsh, J.J., 2007. Displacement transfer between intersecting regional strike-slip and extensional fault systems. J. Struct. Geol. 29, 100–116. doi:10.1016/j.jsg.2006.08.002

Muraoka, H., Kamata, H., 1983. Displacement distribution along minor fault traces. J. Struct. Geol. 5, 483–495. doi:10.1016/0191-8141(83)90054-8

Nicol, A., Watterson, J., Walsh, J.J., Childs, C., 1996. The shapes, major axis orientations and displacement patterns of fault surfaces. J. Struct. Geol. 18, 235–248. doi:10.1016/S0191-8141(96)80047-2

Nilsen, K.., Vendeville, B.C., Johansen, J.., 1995. Influence of regional tectonics on halokinesis in the Nordkapp Basin, Barents Sea., in: Jackson, M.P.A., Roberts, D.G., Snelson, S. (Eds.), Salt Tectonics: A Global Perspective. AAPG Memoir, pp. 413–436.

Omosanya, K.O., Alves, T.M., 2014. Mass-transport deposits controlling fault propagation, reactivation and structural decoupling on continental margins (Espírito Santo Basin, SE Brazil). Tectonophysics 628, 158–171. doi:10.1016/j.tecto.2014.04.045

Peacock, D.C.., Sanderson, D.., 1991. Displacements, segment linkage and relay ramps in normal fault zones. J. Struct. Geol. 13, 721–733. doi:10.1016/0191-8141(91)90033-F

Perez-Garcia, C., Safronova, P.A., Mienert, J., Berndt, C., Andreassen, K., 2013. Extensional rise and fall of a salt diapir in the Sørvestsnaget Basin, SW Barents Sea. Mar. Pet. Geol. 46, 129–143. doi:10.1016/j.marpetgeo.2013.05.010

Pochat, S., Castelltort, S., Choblet, G., Van Den Driessche, J., 2009. High-resolution record of tectonic and sedimentary processes in growth strata. Mar. Pet. Geol. 26, 1350–1364. doi:10.1016/j.marpetgeo.2009.06.001

Reiche, S., Hübscher, C., Beitz, M., 2014. Fault-controlled evaporite deformation in the Levant Basin, Eastern Mediterranean. Mar. Geol. 354, 53–68. doi:10.1016/j.margeo.2014.05.002

Riis, F., Vollset, J., Sand, M., 1986. Tectonic development of the western margin of the Barents Sea and adjacent areas, in: M.T Halbouty: Future Petroleum Provinces of the World, AAPG Memoir. American Association of Petroleum geologists, pp. 661–667.

Schlische, R.W., Anders, M.., 1996. Stratigraphic effects and tectonic implications of the growth of normal faults and extensional basins, in: Beratan, K. K., Ed., Reconstructing the Structural History of Basin and Range Extension Using Sedimentology and Stratigraphy. Geological Society of America Special Publication, pp. 183–203.

Smelror, M., Petrov, O., Larssen, G.., Werner, S.., 2009. ATLAS: Geological History of the Barents Sea. Geol. Surv. Nor.

Stewart, S.A., 2006. Implications of passive salt diapir kinematics for reservoir segmentation by radial and concentric faults. Mar. Pet. Geol. 23, 843–853. doi:10.1016/j.marpetgeo.2006.04.001

Stewart, S.A., Clark, J.A., 1999. Impact of salt on the structure of the Central North Sea hydrocarbon fairways. Geol. Soc. Lond. Pet. Geol. Conf. Ser. 5, 179–200. doi:10.1144/0050179

Stewart, S.A., Coward, M.P., 1995. Synthesis of salt tectonics in the southern North Sea, UK. Mar. Pet. Geol. 12, 457–475. doi:10.1016/0264-8172(95)91502-G

Talbot, C., Koyi, H., Clark, J., 1993. Multiphase halokinesis in the Nordkapp Basin, in: T.O. Vorren, E.B., Ø.A. Dahl-Stamnes, E. Holter, B. Johansen, E. Lie and T.B. Lund (Ed.), Norwegian Petroleum Society Special Publications. Elsevier, pp. 665–668.

Thorsen, C.., 1963. Age of growth faulting in Southeast Louisiana. Trans. Gulf Coast Assoc. Geol. Soc. 13, 103–110.

Tsikalas, F., Faleide, J.I., Eldholm, O., Blaich, O.., 2012. The NE Atlantic conjugate margins, in: Regional Geology and Tectonics: Phanerozoic Passive Margins, Cratonic Basins and Global Tectonic Maps. Elsevier, Amsterdam, The Netherlands, pp. 140–201.

Tvedt, A.B.M., Rotevatn, A., Jackson, C.A.-L., Fossen, H., Gawthorpe, R.L., 2013. Growth of normal faults in multilayer sequences: A 3D seismic case study from the Egersund Basin, Norwegian North Sea. J. Struct. Geol. 55, 1–20. doi:10.1016/j.jsg.2013.08.002

Walsh, J.., Bailey, W.., Childs, C., Nicol, A., Bonson, C.., 2003. Formation of segmented normal faults: a 3-D perspective. J. Struct. Geol. 25, 1251–1262. doi:10.1016/S0191-8141(02)00161-X

Walsh, J.J., Watterson, J., 1987. Distributions of cumulative displacement and seismic slip on a single normal fault surface. J. Struct. Geol. 9, 1039–1046. doi:10.1016/0191-8141(87)90012-5

Wilson, P., Gawthorpe, R.L., Hodgetts, D., Rarity, F., Sharp, I.R., 2009. Geometry and architecture of faults in a syn-rift normal fault array: The Nukhul half-graben, Suez rift, Egypt. J. Struct. Geol. 31, 759–775. doi:10.1016/j.jsg.2009.04.005

Wiprut, D., Zoback, M.D., 2000. Fault reactivation and fluid flow along a previously dormant normal fault in the northern North Sea. Geology 28, 595–598.

Worsley, D., 2008. The post-Caledonian development of Svalbard and the western Barents Sea. Polar Res. 27, 298–317. doi:10.1111/j.1751-8369.2008.00085.x

Xu, S., Nieto-Samaniego, A.F., Alaniz-Álvarez, S.A., Velasquillo-Martínez, L.G., Grajales-Nishimura, J.M., García-Hernández, J., Murillo-Muñetón, G., 2010. Changes in fault length distributions due to fault linkage. J. Geodyn. 49, 24–30. doi:10.1016/j.jog.2009.08.002

Figure

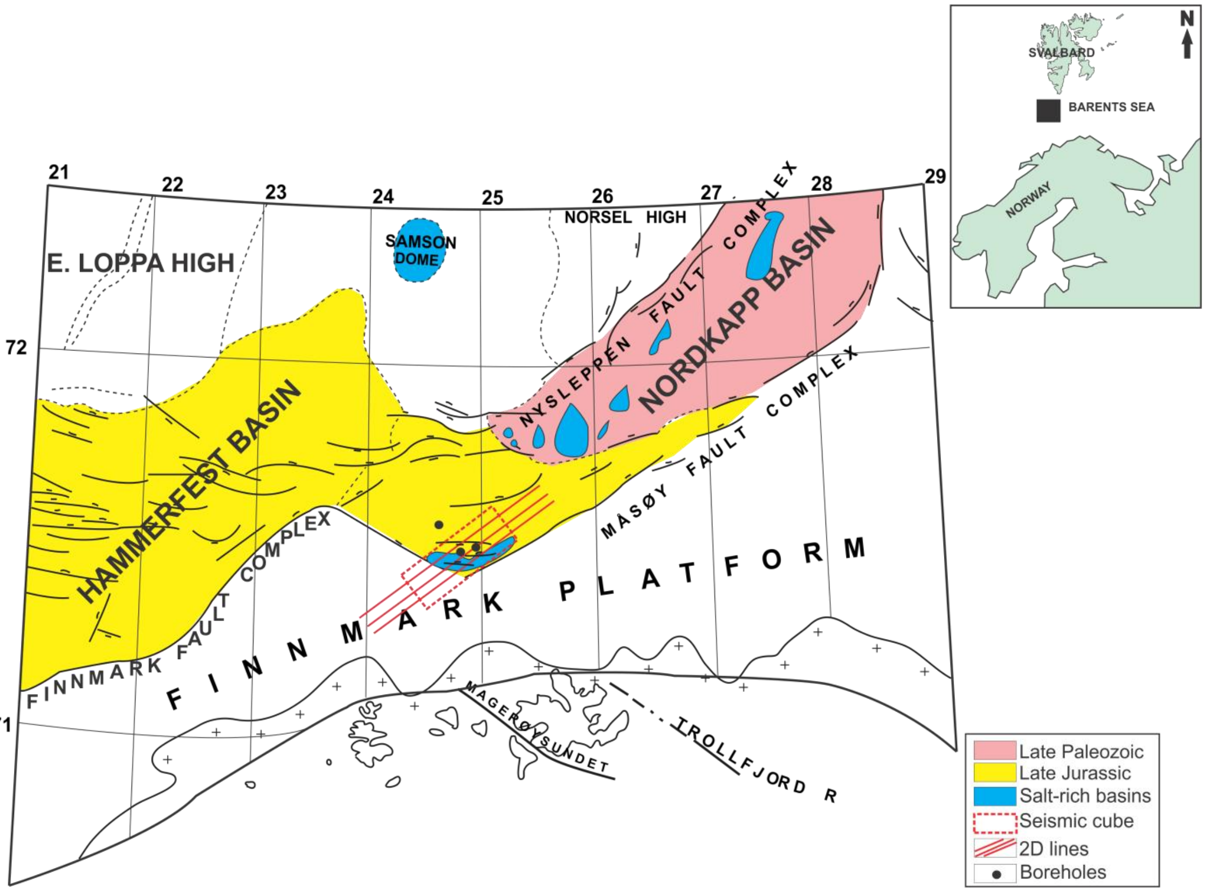

Figure 1a: Geographic location and regional tectonic setting of the Easternmost Hammerfest Basin. Inset shows study area location (modified after the offshore NPD Geological maps of Gabrielsen et al (1990)).

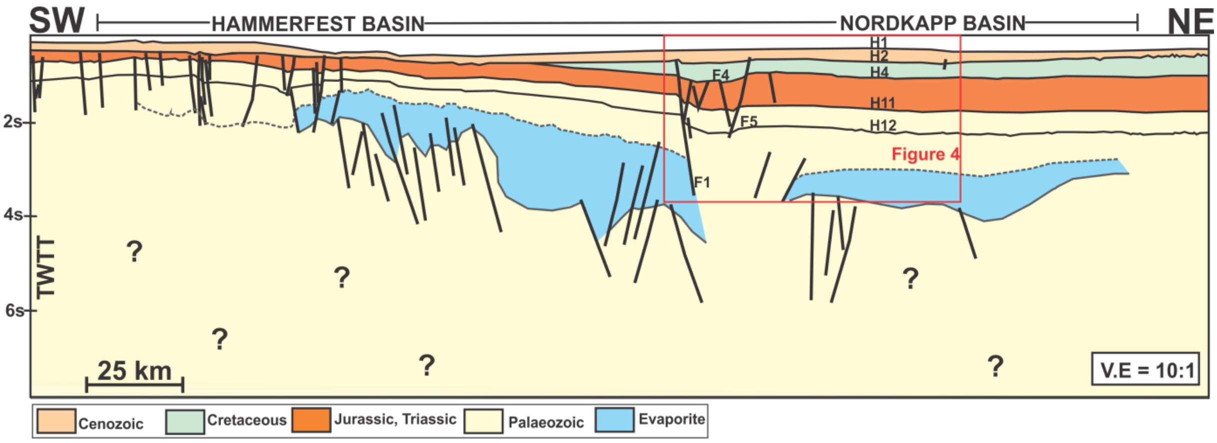

Figure 1b: Regional cross section through the study area. The red rectangle shows the location of the 3D seismic data used for this study. *N.B: The quality of the seismic profile is poor below 5s.*

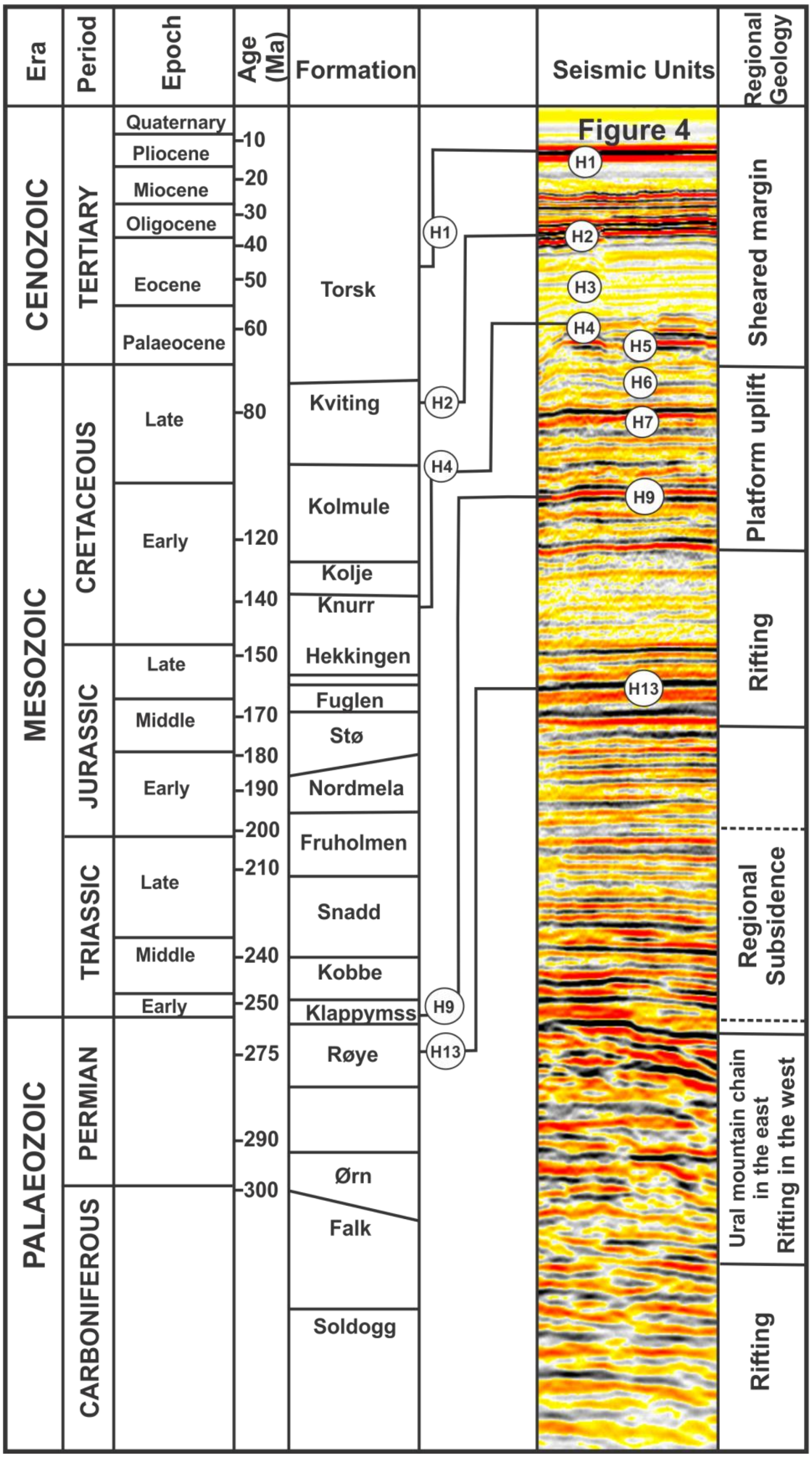

Figure 2: Litho- and seismic stratigraphy column of the study area. The units are divided based on interpreted horizons H1 to H15 and their stratigraphic correlatives of Mørk et al., 1999 and Glørstad-Clark et al., 2010. Interpreted horizons in the study area correspond to the tops of Cenozoic, Cretaceous, Jurassic, Triassic and Paleozoic strata. Evaporites in the study area were deposited during the Carboniferous and Triassic times.

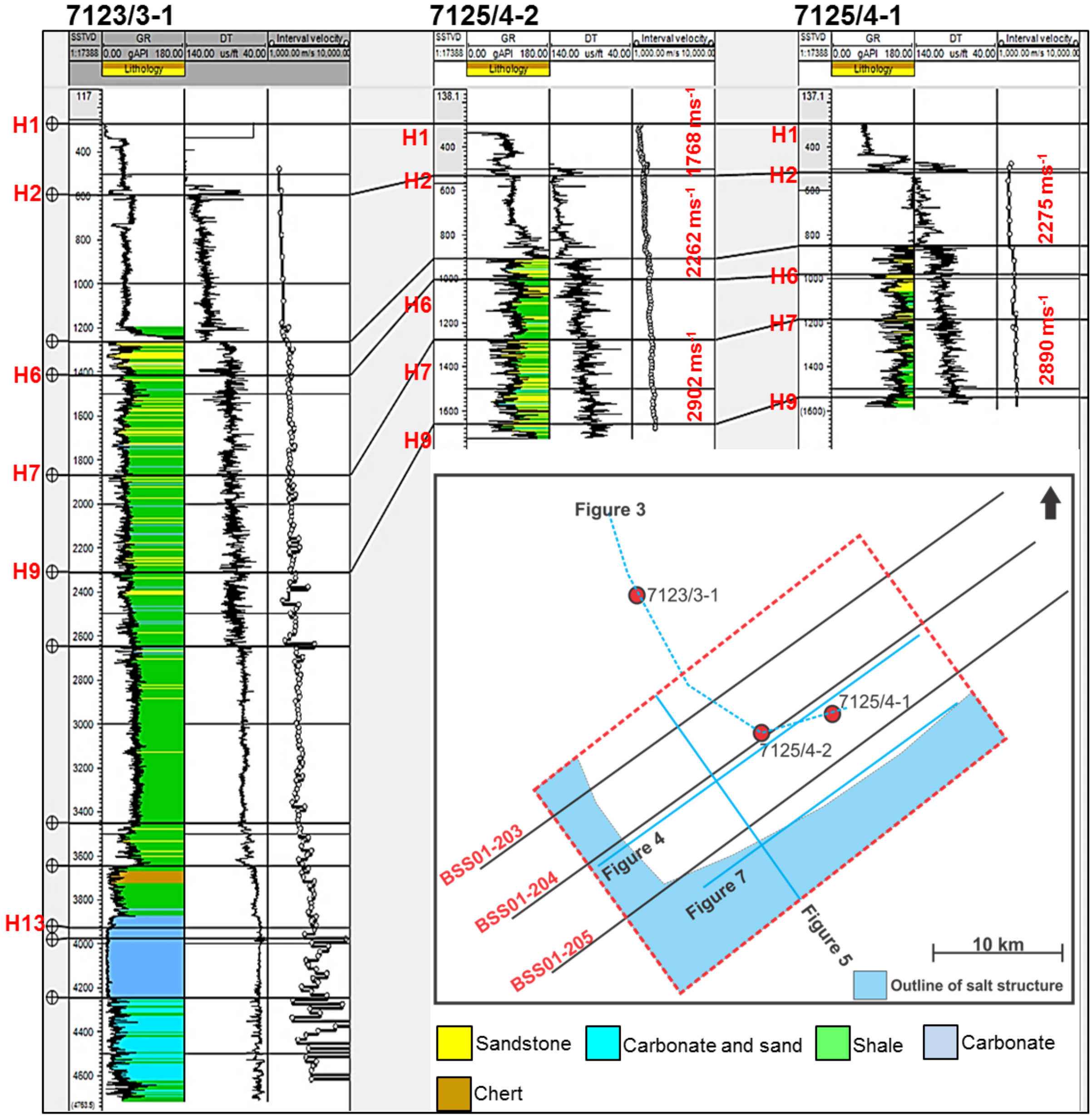

Figure 3: Correlation panel for lithology and age correlation in the study area. Also shown is the interval velocity used for depth conversion. *Inset: outline and location of the seismic sections discussed in the text.*

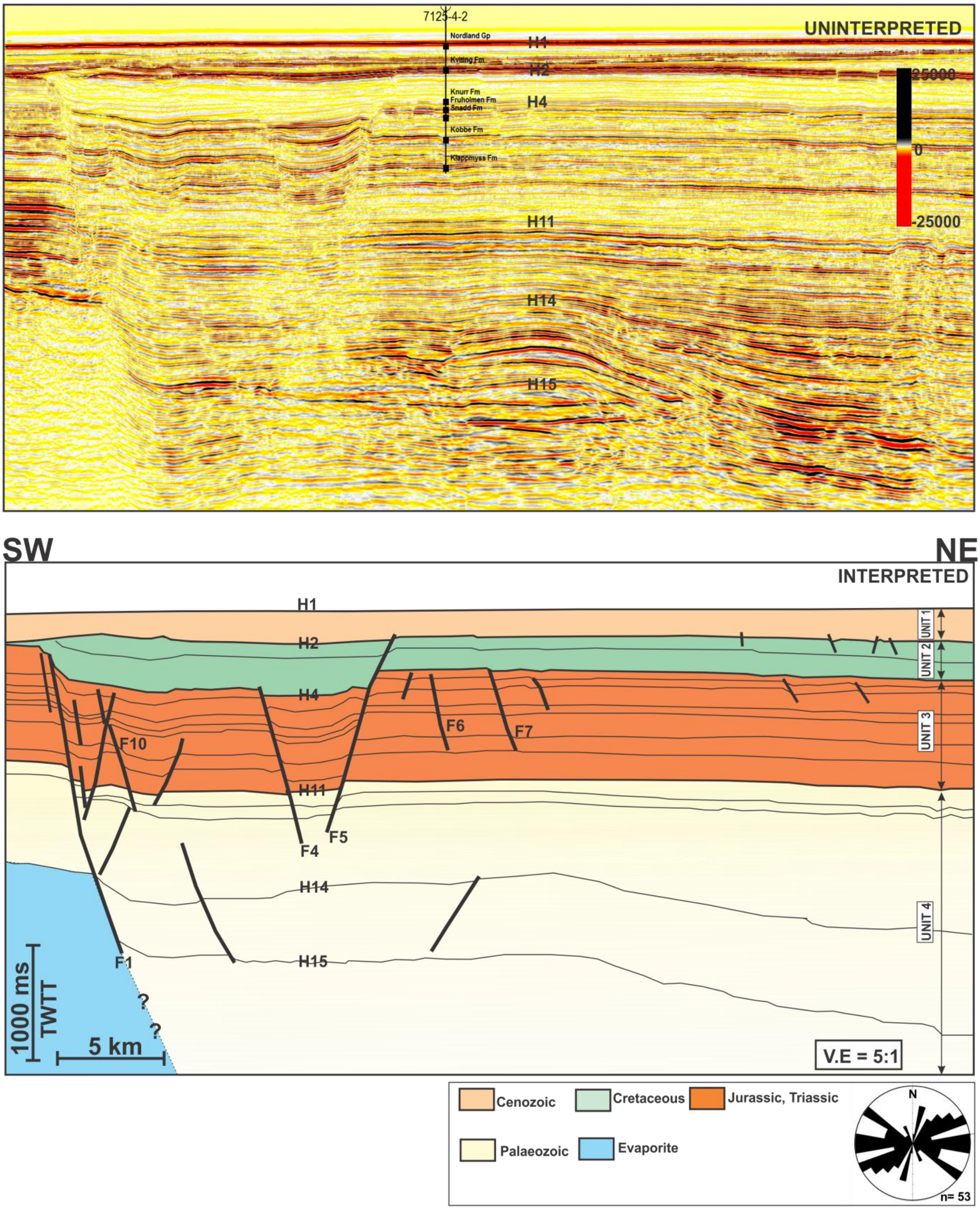

Figure 4: Uninterpreted and geoseismic section showing some of the interpreted faults. Faults in the study area include normal faults restricted to Paleozoic strata, Jurassic and Triassic faults whose upper tips are truncated by the H4 unconformity, fault extending into the Cretaceous interval. Fault geometry includes graben, half-graben, synthetic and antithetic faults. The rose diagram shows the orientation of all the fifty-three faults discussed in the text. *See Figure 7 for location of seismic profile.*

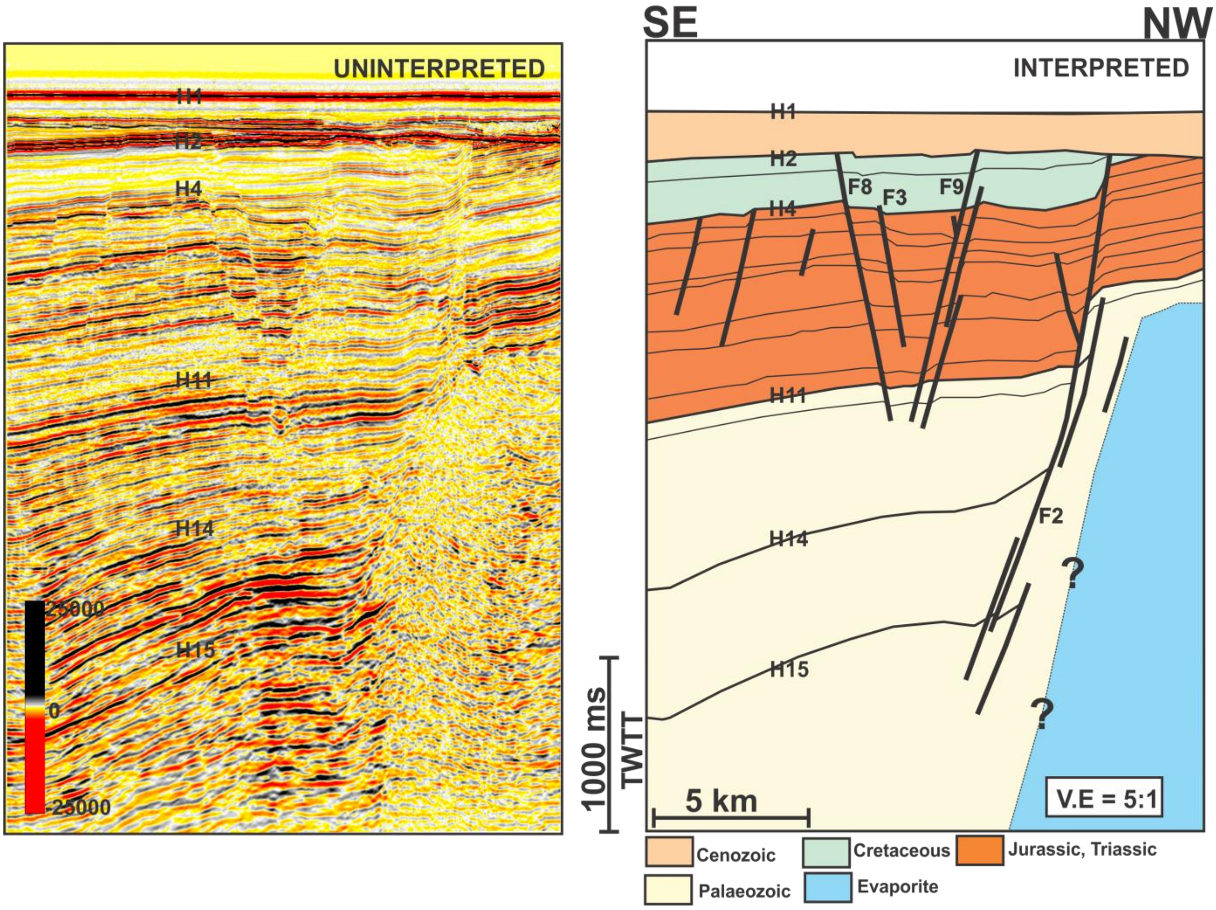

Figure 5: SE to NW uninterpreted and geoseismic section showing examples of other faults in the study area. Fault with the label are used for displacement analysis. The seismic section revealed complex faulting within the lower Paleozoic interval. Faulting at this stage is attributed to the initial phase of salt flow. Fault, F2 shows possible dip linkage character towards its lower tip. N.B: *On seismic the boundary of the evaporite is marked by significant change in amplitude character of the reflectors.*

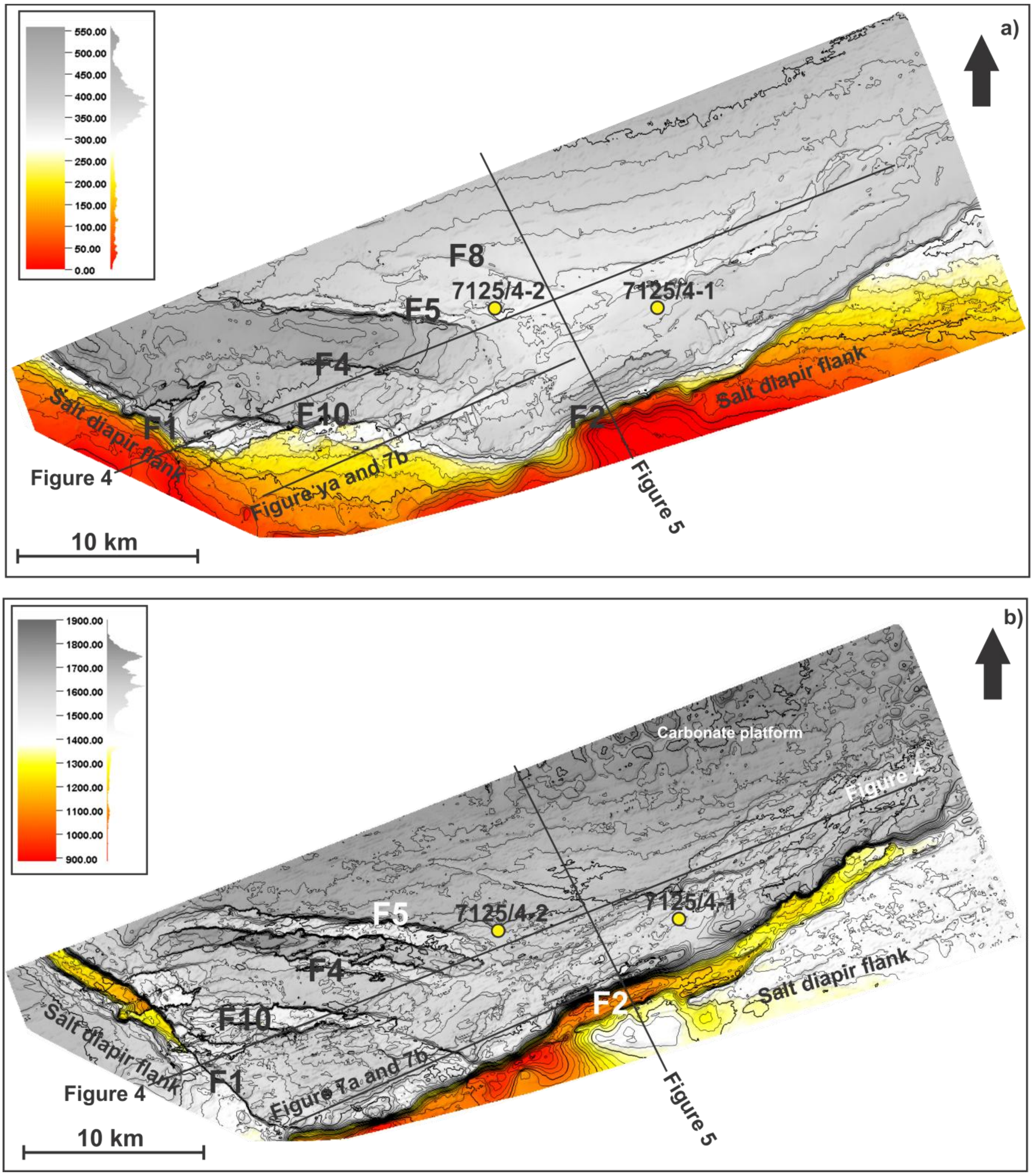

Figure 6: Isopach map for the thickness of the stratigraphic units between (a) H2 to H4, small-scale faulting in the western part of the map is expressed as subtle uplifted and subsided block and (b) H4 to H13. Faulting of pre- Cretaceous units is expressed as thickness variation across faults N.B: *The black line shows the location of the seismic profile shown in Figures 4, 5 and 7 while the yellow-filled circle shows the position of the two boreholes used for depth conversion and lithostratigraphic correlation.*

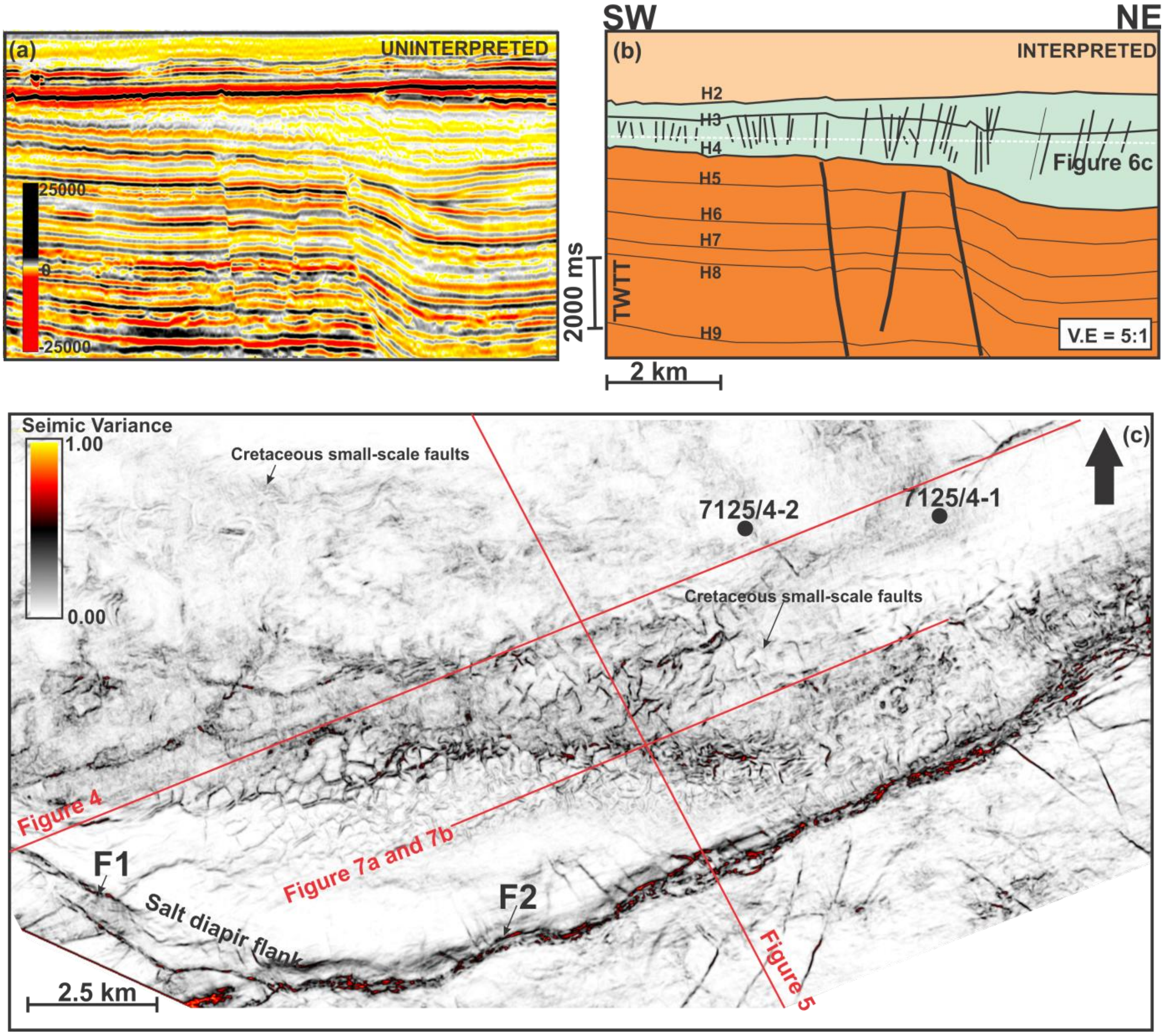

Figure 7: (a) and (b) Uninterpreted and geoseismic section showing subtle faults within the Cretaceous interval (c) Variance slice at -764 ms (TWTT) shows the map view of the interpreted faults in Figure 6b. The faults have polygonal-shape in plan view, they are characterized by subtle offset of the H3 horizons and do not extend up to the H2 and H4 horizons, respectively.

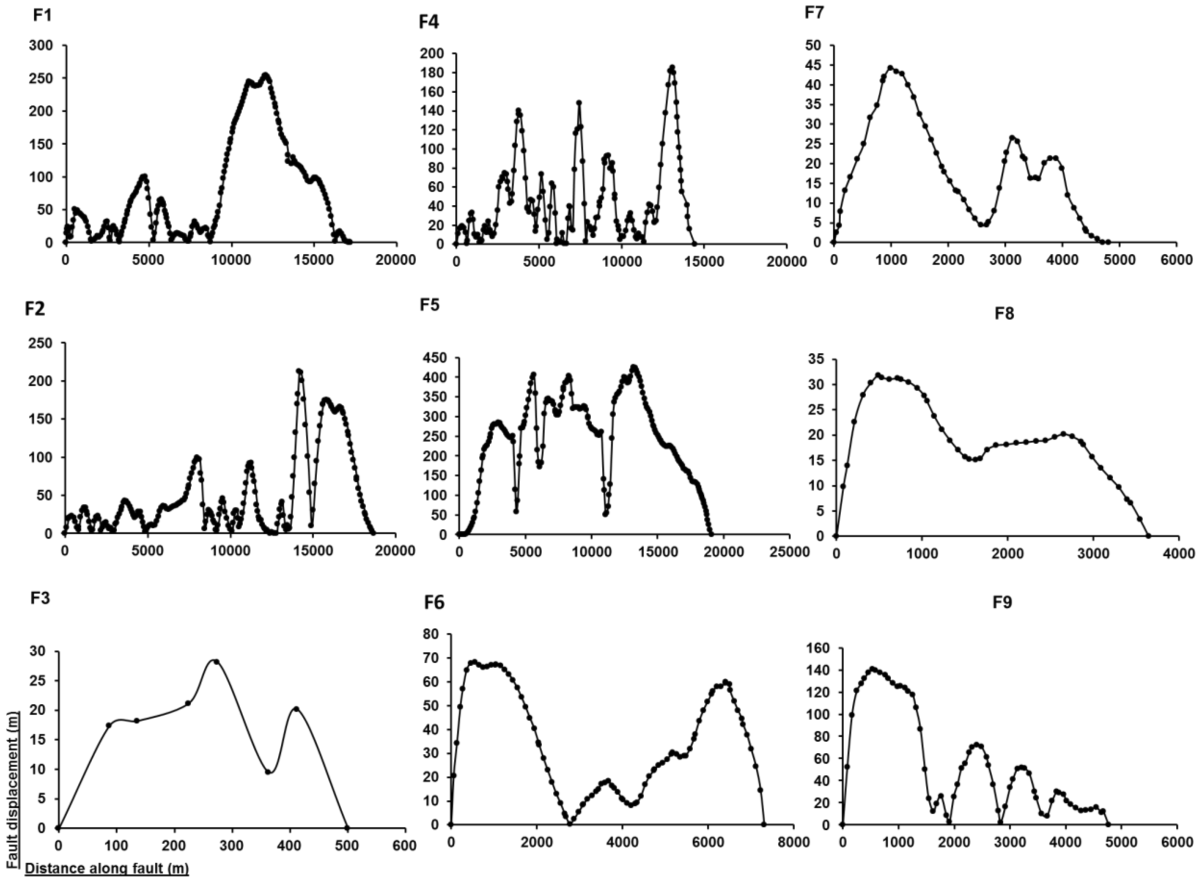

Figure 8: Displacement (d) versus distance (x) plots includes c-type, m-type and hybrid profiles. The curves were made along the horizon, H5.

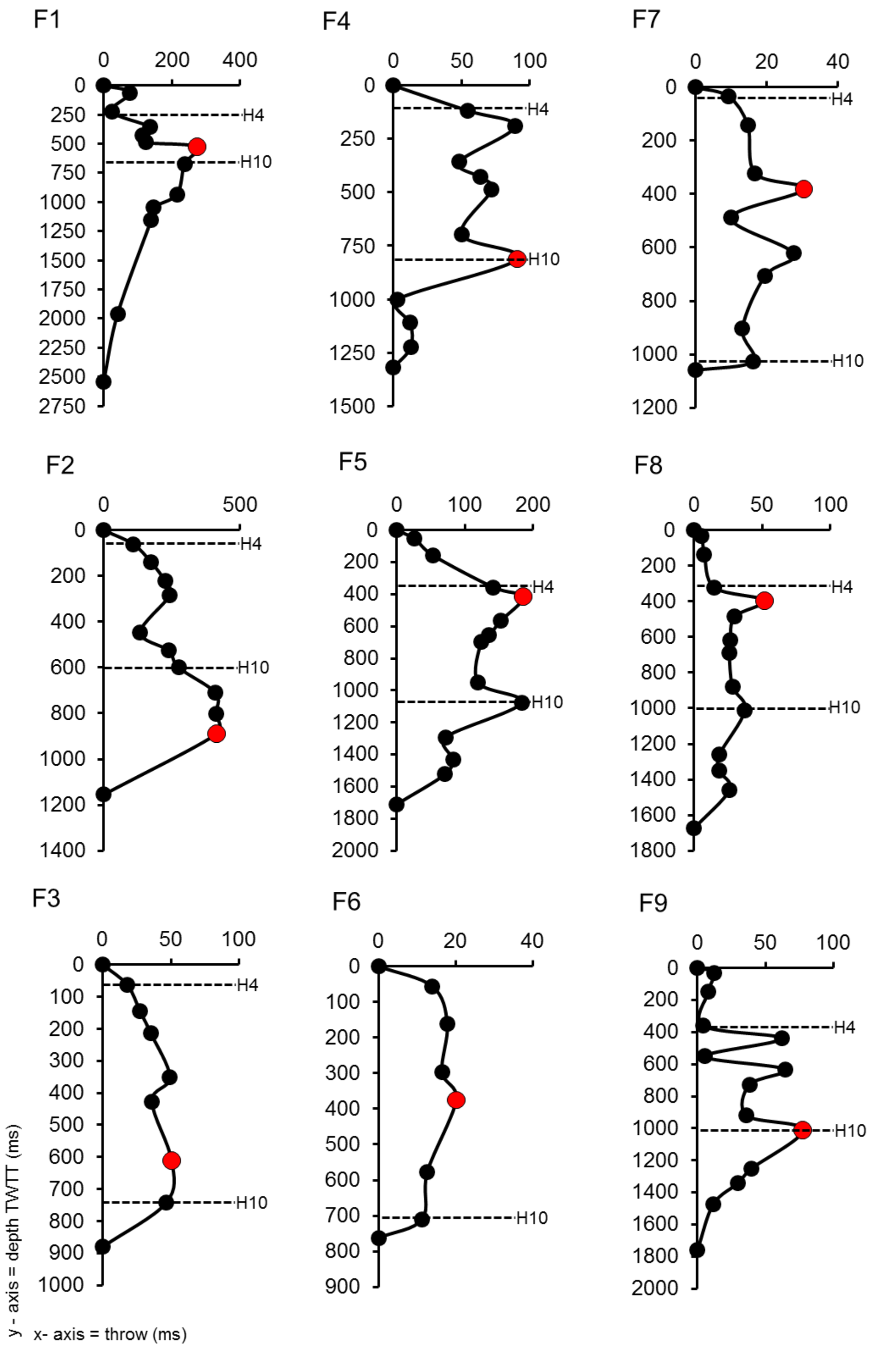

Figure 9: Throw (t) versus depth (z) plots for representative faults in the study area. The throw profiles include C-type, M-type, Skewed M-type and Asymmetrical profiles of Muraoka and Kamata, 1983. N.B: *The red-filled circle shows the position of maximum displacement (d max) for each of the fault and TWTT – Two-Way Travel Time.*

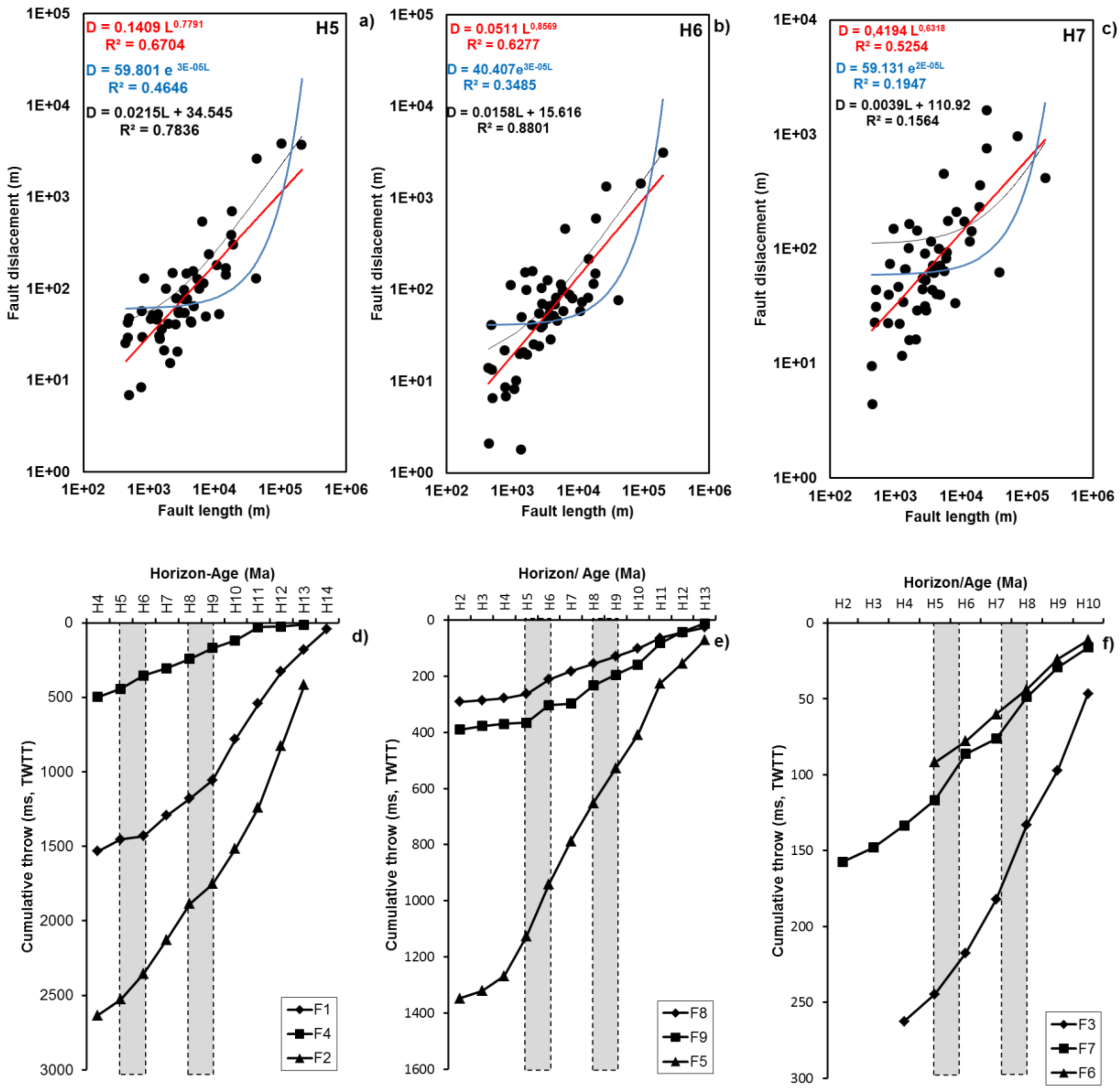

Figure 10: (a-c) Displacement scaling for all the fifty-three faults interpreted in the study area revealed a power-law relationship with an exponent ~1. The correlation coefficient for the best-fit curve ranges from 0.5 to 0.7 (e-f) plot of cumulative throw against age of horizon intersected by the nine representative faults. Skips or steps on the curve are interpreted as period of fault reactivation. N.B: *The grey zone marks the location of the prominent skips.*

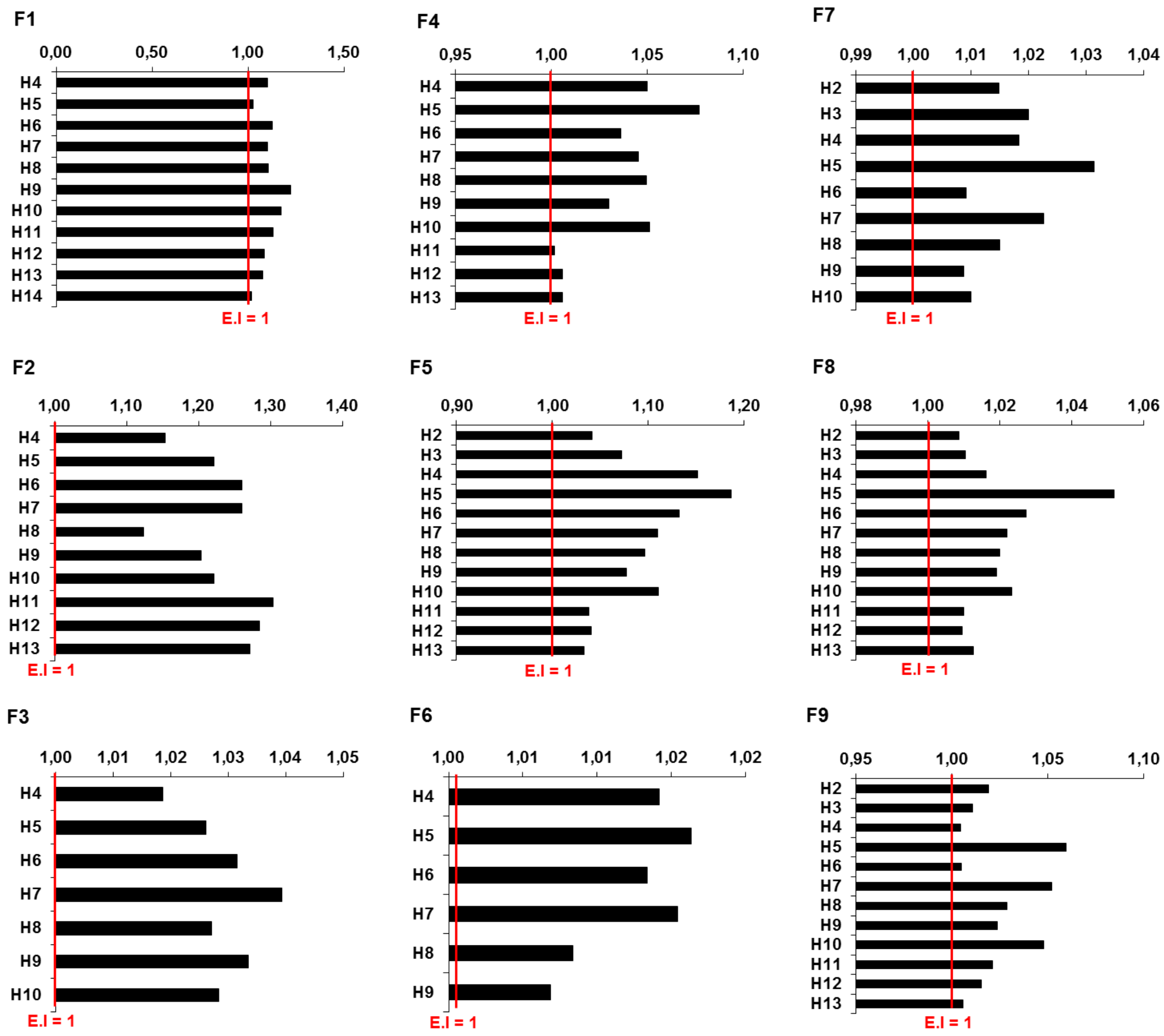

Figure 11: Expansion index (EI) for the faults include EI > 1 suggesting significant thickening of strata on the downthrown side of the faults and EI < 1 associated with thinning of sediments in the hanging wall of the faults (Thorsen, 1963; Pochat et al., 2009). Faults in this study area characterized by EI >1. N.B: *The red line marks the position of expansion index equivalent to 1.*

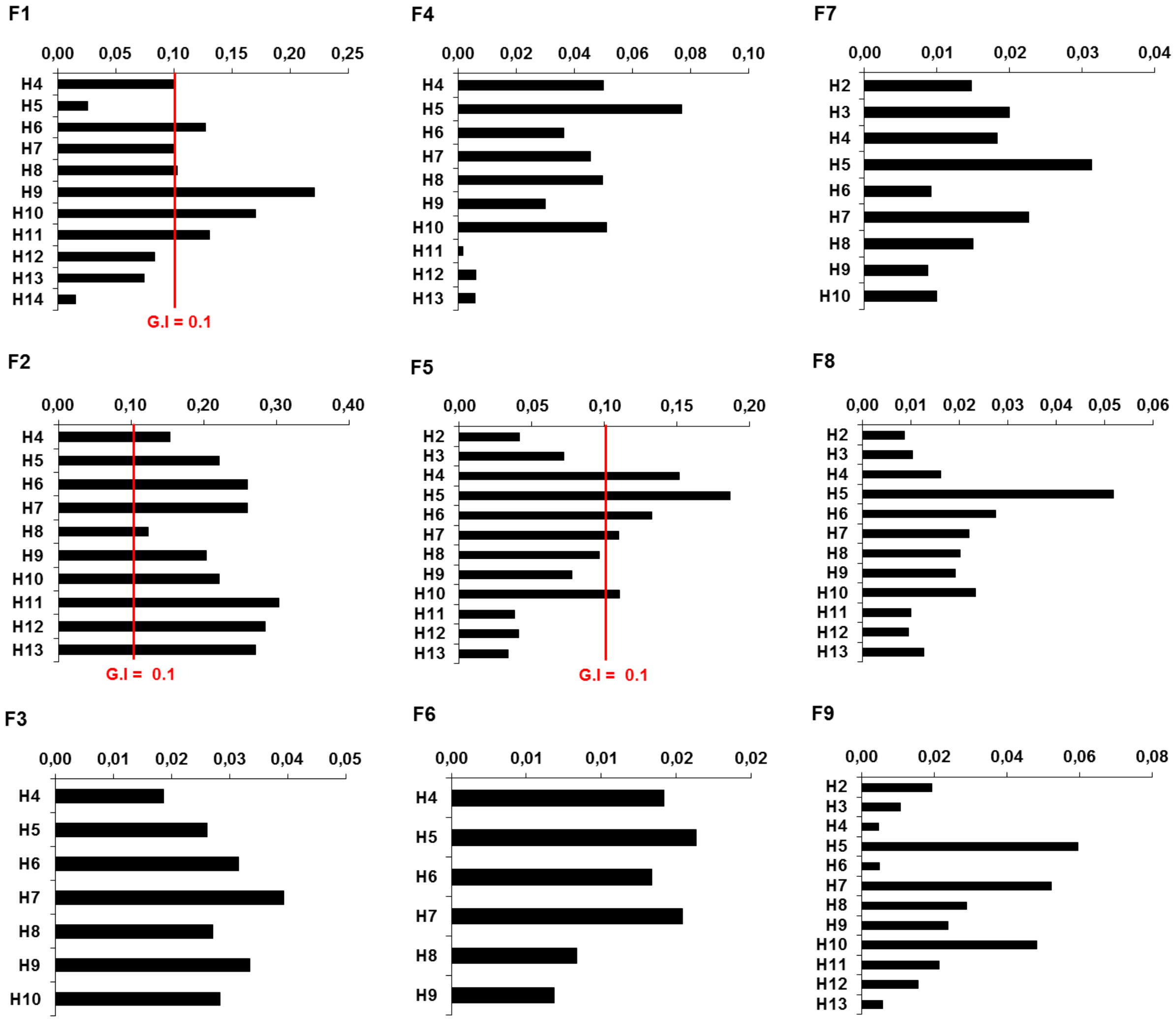

Figure 12: Faults in the study area have growth index (GI) of > 1 and < 1. GI of > 1 implies the faults were buried beneath stratigraphic surfaces during their growth while GI < 1 indicate the faults grew to the surface and interacted with a free surface. N.B: *The red line marks the position of growth index equivalent to 1.*

Table

Table 1: Seismic character of the principal horizons defining the units described in section 4

Unit	Upper Boundary	Description	Lower Boundary	Description	Well top	Age
1	H1	Continuous high amplitude reflector	H2	Oligocene unconformity represents the base of the unit. H2 is high amplitude and continuous surface.	Seabed to Kviting Fm.	Cenozoic
2	H2	Continuous moderate to high amplitude and moderately faulted reflection	H4	Base Cretaceous unconformity	Kviting to Knurr Fm.	Cretaceous to Jurassic
3	H4	Continuous low to moderate amplitude	H11	High amplitude reflection	Knurr to Mid. Klappymss	Triassic to Paleozoic
4	H11	Continuous high amplitude reflection	Limit of data	High amplitude reflections	Mid Klappymss to Paleozoic	Paleozoic